Post-processing image techniques for experimental methods in thermography

José Mendes

josefranciscopm@tecnico.ulisboa.pt

Instituto Superior Técnico, Universidade de Lisboa, Lisboa, Portugal

December 2021

Abstract

Thermography allows for the capture of thermograms, matrices with the values of temperature, in a non-invasive way and with a high temporal resolution. This technique is adequate for the study of heat transfer phenomena. Nevertheless, in order to obtain thermograms with high accuracy, it is necessary to use an adequate methodology. The methodology proposed in this work, allows the user to infer several parameters that affect the precision and accuracy of the measured values: the shape factor, the emissivity of the material and the relation between ADU and temperature. In addition to this a number of post-processing techniques for thermograms are analysed, emphasising the results of NUC, used for the proposed methodology. In addition to the post-processing of thermograms, an approach to the computation of heat flux using neural networks is proposed, intended to compute the heat flux in pool boiling experiments. The experimental results obtained with the new methodology are compared with the ones obtained using the methodology currently in use in the laboratory. The new methodology's thermograms present good results, with a smaller nonuniformity than the thermograms treated with the previous methodology. The approach to the heat flux's computation also presents values with less oscillation and better reliability in determining the peak flux caused by the bubble detachment from the surface.

Keywords: Thermography, Non-uniformity correction, Neural networks, Heat flux, Pool boiling

1. Introduction

Heat transfer is a common phenomenon, observed in several industrial applications. As such, there is a large interest in studying and characterising it in order to improve processes. On account of the phenomena complexity and the small time window in which they occur specific techniques are required to study them.

Thermography is a non-invasive technique, with high temporal resolution and that measures two-dimensional data, ideal for the study of heat transfer mechanisms. There are several methods for the acquisition and processing of thermal images, with some being integrated directly on the cameras. However, they require a correct assessment of several parameters related to the scene and the camera. The accuracy of the results is directly influenced by these parameters. These processing methods treat thermograms, not images, which requires care in order to maintain the accuracy of the temperature values.

In the present work a methodology for the acquisition and post-processing is presented, alongside comparisons with the methodology currently in use in the laboratory. Furthermore, an approach that resorts to neural networks, in order to compute the heat flux in a pool boiling configuration is proposed and the results analysed.

In section 2, the theoretical background of infrared thermography is analysed as well as the specifics of the camera utilised in this work. In section 3, two treatments for the processing of thermal images are presented and compared. Both methodologies procedures and the experimental setup are presented in section 4. The results obtained are presented in section 5. The conclusions and proposed future work are presented in section 6.

2. Background

2.1. Thermography

Although thermography is commonly refereed as measuring temperature values, thermographic cameras measure infrared radiation values. These values can be converted to temperature values, with the accounting of other parameters related to the recorded scene.

The camera infrared sensor receives radiation from several sources presented in the following equation [4]:

$$\Phi_{measured} = \tau\mathcal{E}\Phi(T) + \tau(1-\mathcal{E})\Phi(T_{env}) + \\ + (1-\tau)\Phi(T_{atm}) \quad (1)$$

Where $\Phi(T)$ corresponds to the radiation, related to the temperature, T. The first term, $\tau\mathcal{E}\Phi(T)$, corresponds to the radiation emitted by the observed body, $\tau(1-\mathcal{E})\Phi(T_{env})$, corresponds to the radiation emitted by the surroundings and reflected by the body, with τ as the atmosphere transmittance coefficient. The last term, $(1-\tau)\Phi(T_{atm})$, corresponds to the radiation from the atmosphere between the body and the infrared sensor.

In order to relate the temperature, T and measured radiation Φ the following equation is employed, as suggested in [4]:

$$\Phi(T) = \frac{R}{e^{B/T} - F} + O \quad (2)$$

The B, F, R and O are the standardised constants. Since the experimental setup is not ideal, the distance of the camera from the scene influences the measured value. The shape factor, F_{1-2}, quantifies this discrepancy, where 1 refers to the emitting body radiation received by 2, the camera sensor.

Utilising equations 1 and 2, the following equation is obtained:

$$T = \frac{B}{Ln\left(\frac{R}{\alpha - O} + F\right)} \quad (3)$$

$$\alpha = (\Phi_{measured} - \tau(1-\mathcal{E})\Phi(T_{env}) - \\ (1-\tau)E(T_{atm}))/(\mathcal{E}F_{1-2}\tau) \quad (4)$$

Since conditions in the laboratory are controlled, the ambient and environment temperature is constant between experiments. This allows for the simplification of the temperature and radiation relation to the following expression, with the inclusion of the environment and atmosphere radiation terms in the standardised constants:

$$T = \frac{B}{Ln\left(\frac{R}{\frac{\Phi_{measured}}{\mathcal{E}F_{1-2}} - O} + F\right)} \quad (5)$$

With equation 5 it is possible to convert the intensity values measured by the camera to temperature values.

2.2. Heat flux computation

In order to analyse the thermal phenomena, the experimental configurations included a thin metallic foil under the phenomena in order to apply the following heat flux equation, formerly utilised by [6] and [8]:

$$q = q_0 + k_h\delta\left(\frac{\partial^2 T}{\partial x^2} + \frac{\partial^2 T}{\partial y^2}\right) - \rho_h c_{p,h}\delta\frac{\partial T}{\partial t} \quad (6)$$

Where q is the heat flux, q_0, the imposed flux, k_h, ρ_h and $c_{p,h}$ the conductivity, density and specific heat of the foil, and δ is the foil thickness.

2.3. Neural networks

One of the uses of neural networks is function approximation. As such they approximate the thermogram surface, resulting in a smoother surface than the original. The utilisation of smoothed thermograms is useful for the heat flux computation since equation 6 derivatives amplify the thermograms noise.

The neural networks employed in this work were feedforward neural networks, trained with the Levenberg–Marquardt algorithm. The networks were made up of two layers: a first layer with several radial base neurons and a second layer with a single linear neuron. The number of neurons of the first layer impacts the complexity of the surface with each neuron corresponding to a dome in the surface. The second layer combines the aforementioned domes reproducing the thermogram surface. As such these neural networks have two main adjustable parameters: the number of neurons in the first layer and the target error.

2.4. Super resolution

On account of the spatial resolution of the thermograms, the increase in resolution allows for the extraction of important information. To do so a spatial interpolation of the values is performed, obtaining bigger data arrays which contain the original points and additional interpolated points. This allows for the display of less pixelated images and definition of more fluid contours.

The utilisation of this technique needs to be planned. Owing to the use of interpolation, the derivatives of resolution increased thermograms may contain optic artefacts, creating aberrations in the computed heat flux. The increase in memory is also significant with an increase requiring a $3^2 = 9$ increase of the memory usage for the super resolution thermal video, because of the increase in both spatial dimensions.

2.5. Infrared camera

The thermal camera utilised in the present work was a *Xeneth* camera, model *Onca-MWIR-InSb-320*. This camera has an infrared focal plane array (IRFPA) with a resolution of 320 by 256 pixels. The array material, indium antimonide (InSb), requires cooling to a $80\,K$ temperature, accomplished by the incorporated Stirling engine.

The camera sensors signal is converted to digital units by a 14 bits converter, with two extra bits added for data storage. These extra bits do not contain extra data and are added differently depending on the software employed.

The camera integration time, analogue to the exposure time in photography, influences the analogue to digital units (ADU) value measured. As such the choice of integration time needs to account for the temperatures to be measured.

The region of interest (RoI) of the camera defined by the software allows for an increased framerate, caused by the reduction of information to be transferred. This option is important to obtain the required temporal resolution to the study of heat exchange phenomena.

Besides the aforementioned parameters, integration time and RoI, the camera has several other options. An anti-bloom option prevents the saturation of the measured values, when exposed to a small source of intense radiation, using an unknown algorithm. Since this algorithm changes the measured values in an unknown way the option is disabled in order to obtain a signal with the least processing. The global sensor array has an adjustable gain and bias, that influence the values measured. These values remained the same throughout this work. Another camera option is the calibration pack, which affects the camera performance. These pack usage is presented in the methodologies section 4

Figure 1 presents a thermogram without any treatment. In the thermogram a computer monitor is shown, distinguishable from the surroundings due to its higher temperature.
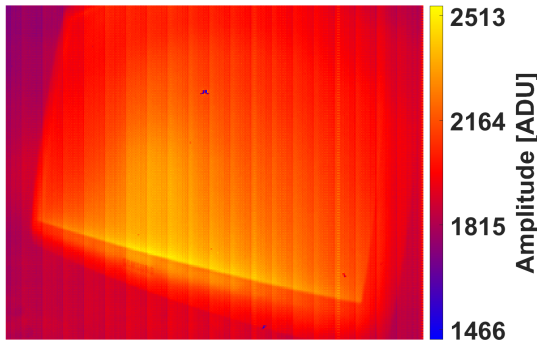

Figure 1: Thermogram with pattern noise

As presented in figure 1, the thermogram has a patterned noise, mainly vertical stripes pattern, that degrades the acquired data. In order to minor this noise, the camera has an integrated option of offset calibration. The camera software requires a constant temperature and emissivity surface as reference in order to perform the correction. This treatment is effective when the camera has the full IRFPA selected as RoI. If the selected RoI is smaller, performing the offset correction causes horizontal stripes to appear in the thermograms, further deteriorating the data quality.

The camera was connected to the computer in two ways: via CameraLink with a National instruments board and via Ethernet cable. On the computer side, the data acquisition was performed by several software: the board software, NI-MAX, the camera software, Xeneth, and Matlab. The pattern noise is present in all the connections combinations. The horizontal stripes only appear after a RoI change and offset correction with the Xeneth software, but can be seen if the camera is connected without reset with any other method. As such the connection method and software used is of importance since it influences the noise present on the captured thermograms.

The pattern noise had a constant amplitude for different radiation exposure levels. By increasing the scene temperature the pattern noise became less noticeable in the visual representation of the thermograms, but still deteriorated and affected the heat flux computations.

3. Thermogram treatment methods

The existing methods to improve the thermograms are divided into two fields: Non-uniformity corrections, utilising calibrated images and scene based techniques. In this section the theoretical background and experimental results of the two of methods with most promising results are presented.

3.1. Non-uniformity correction

The Non-uniformity correction (NUC), [5] requires calibrated images of uniform radiation to correct the thermograms. Depending on the available number of references, the correction utilises one, NUC1, or two, NUC2 calibrated images.

In both cases, each pixel of the IRFPA is assumed to have a linear response, with different bias and gains for each pixel, i, j, creating the pattern noise. In order to create a uniform thermogram the following equation is applied to each reference:

$$V_{i,j}(\Phi_k) = \overline{V}(\Phi_k) \qquad (7)$$

Where V is the value of the individual pixel response when subject to the uniform radiation Φ. $\overline{V}$ represents the spatial average of all pixels in the calibrated image.

The linear correction of the non-uniformity is described by the following equation:

$$Y_{i,j} = K_{i,j}V_{i,j} + b_{i,j} \quad (8)$$

Where Y is the corrected value, K a gain matrix and b a bias matrix.

In the case of NUC1, only one reference was used. In order to solve equation 8, with equation 7, the gain K was set to a unitary gain, simplifying the resulting equation:

$$Y_{i,j}(V_{i,j}) = V_{i,j} + b_{i,j} \quad (9)$$

With the bias given by:

$$b_{i,j} = \overline{V}(\Phi_1) - V_{i,j}(\Phi_1) \quad (10)$$

With 1 as the index of the selected reference.

In the case of NUC2, two references were required. Equation 8 is solved, applying equation 7 at two points obtaining the following bias and gain matrices:

$$\begin{cases} K_{i,j} = \frac{\overline{V}(\Phi_2) - \overline{V}(\Phi_1)}{V_{i,j}(\Phi_2) - V_{i,j}(\Phi_1)} \\ b_{i,j} = \overline{V}(\Phi_2) - K_{i,j}V_{i,j}(\Phi_2) \end{cases} \quad (11)$$

Where index 1 and 2 represent each reference.

In both cases, because of equation 7, the corrected thermogram for the reference intensity produced a flat surface. As the measured value drifted from the reference value, the correction lost effectiveness. As such the reference images utilised need to take into account the temperature range of the experimental configuration.

3.2. Constant statistics

The constant statistics (CS) algorithm [2] is a scene based algorithm, as such, it does not require reference images to remove the pattern noise. Since the calibrated images utilised for NUC methods are difficult to obtain, requiring frequent adjustment owing to time drift of the parameters, CS appears as algorithm able to adapt to the scene presented in each video.

Biological adaptations change the perception of a scene. In the case of staring at the same colour for some time, the saturation of the colour is perceived as decreasing. One theory to explain this effect is that colour perception operates under the following constraint: that the average colour perceived is grey. Inspired by biological systems, the CS algorithm applies the following constraints to the thermal videos [2]:

- The average pixel intensity is identical

- The variance of the input of each pixel is identical

These constraints are true for the average moving real world object, but when a static scene is recorded these assumptions are violated.

Considering a linear sensor, the signal is given by the following equation [2]:

$$x = \frac{y - m_y}{s_y} \quad (12)$$

Where y is the registered signal and x is the original signal, changed by a gain m_y and a bias s_y.

Without loss of generalisation, assuming an average signal mean as zero and a unitary standard deviation of the original signal, the signal is recovered by computing m_y and s_y. These variables can be computed recursively, for discrete time, using the following equations, with n as the current instant[2]:

$$\hat{m}_y = \frac{y(n) - (n-1)\hat{m}_y(n-1)}{n} \quad (13)$$

$$\hat{s}_y = \frac{|y(n) - \hat{m}_y| + (n-1)\hat{s}_y(n-1)}{n} \quad (14)$$

On account of the low computational cost this method is able to correct thermal videos in real time.

Since the experimental configurations violate the assumptions for this algorithm, the resulting videos have the permanent objects "burned in" even after the object moved, like ghosts. To counter this effect a de-ghosting module was implemented [3]. To achieve this the de-ghosting module detected the change in mean and variance of the signal, comparing it to a threshold value, and only updated them in case the change was greater than the threshold. The authors of this module [3] proposed a 10% to 25% threshold, with a 20% threshold value being used in this work.

This algorithm recovered a signal with zero mean and a unitary standard deviation, removing a crucial part of the signal information.

3.3. Comparison

In order to compare the NUC and CS algorithms, a comparison between NUC1 and NUC2 is presented. The following index describes the thermogram non-uniformity [7]:

$$UN = \frac{1}{\overline{y}}\sqrt{\frac{\sum_{i=1}^{M}\sum_{j=1}^{N}[y_{i,j} - \overline{y}_{i,j}]^2}{M \times N}} \quad (15)$$

With UN the measure of non-uniformity, y the signal, and M and N as the two spatial dimensions of the thermogram. In order to reduce non-uniformity this measure should be minimised, with zero corresponding to a uniform thermogram.

Figure 2 presents the non-uniformity of the corrected thermograms for both NUC. The thermograms were acquired while the cell from the configuration presented in section 4.3 cooled, with the recorded surface cooling at a uniform temperature.
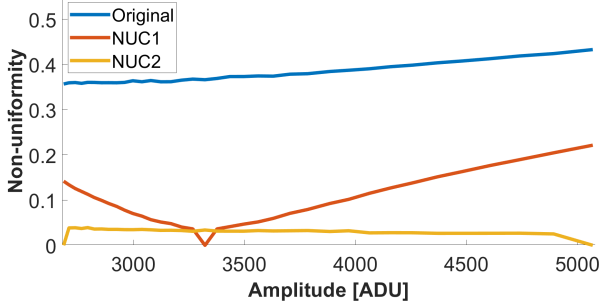

Figure 2: Non-uniformity values for different intensity uniform thermograms

As stated in section 3.1, both corrections eliminated the non-uniformity at the reference used in the correction. In the case of NUC1 this was at 3300 ADU. For NUC2 the null values were at 2700 ADU and 5100 ADU. When the ADU values changed from the reference the NUC1 UN values quickly surpassed the NUC2 values. As for NUC2, the UN value remained at lower levels, with more uniform thermograms. For this reason, the NUC2 should be preferred to NUC1, if two calibrated images can be obtained. As such the NUC2 was used for comparison between non-uniformity correction methods and scene based methods.

To compare both methods, an experiment with the configuration presented in section 4.3 was performed. In the original image, the pattern noise was visible, figure 3, with a lower intensity circular area, corresponding to the orifice where the foil was visible. In this region, the bubble was not noticeable, with the orange region corresponding to a surface defect.
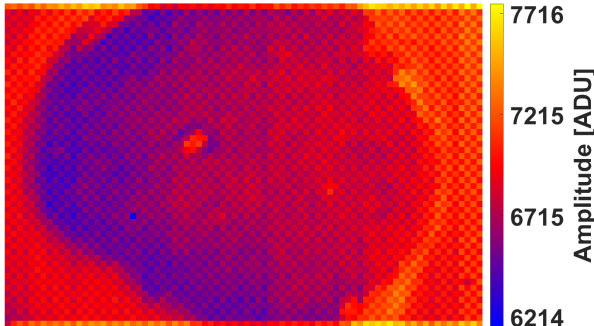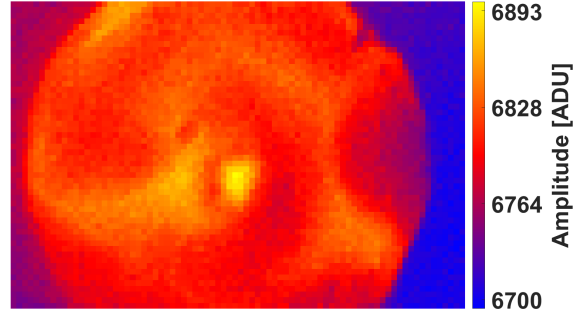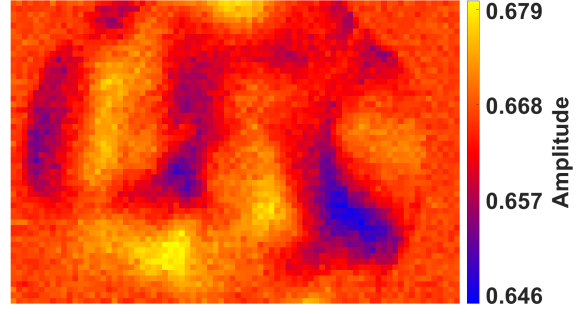

Figure 3: Thermogram before processing

Figures 4(a) and 4(b) present the treated thermograms using NUC2 and CS algorithms respectively.

(a) NUC2

(b) CS with the de-ghosthing module

Figure 4: Comparison between NUC2 and CS

As expected, both algorithms presented in figure 4 removed the pattern noise. The circular region with the foil was highlighted from the rest of the thermogram with both methods. Nevertheless owing to the fixed nature of the scene the CS algorithm did not show the bubble.

The bubble was clearly visible in the NUC treated thermogram. In addition to this, the NUC method did not distort the ADU values of the thermogram, keeping the spatial average from the original. For these reasons, the NUC was the method selected for the proposed methodology.

4. Methodology and experimental configuration

4.1. Previous methodology

This methodology, currently in use in the laboratory, was proposed in [6]. It utilised the camera *Onca-MWIR-InSb-320*, connected to the computer using the cameralink. The video acquisition was performed with the Xeneth software. Before the acquisition a specific calibration pack was selected, in order to minimise non-uniformity effects. The integration time must be set to $200\,\mu s$, after which the software offset correction was performed. This correction was similar to a NUC1, requiring a scene with uniform radiation. After this procedure, the camera was ready to record.

Besides capturing the main video, this methodology required an auxiliary video of a scene at a uniform temperature for the post-processing routine. The temperature of the scene must also be registered.

5

The videos from the camera are stored in the Xeneth native *.xvi* format and needed to be converted to *.avi* so that the Matlab script could read them. This script began by converting the ADU value to the radiation value in order to compute the temperature value with an equation similar to equation 1. The ADU value was converted to a radiation value utilising a fourth degree equation:

$$A \times \Phi^3 + B \times \Phi^2 + C \times \Phi + D = ADU \quad (16)$$

After the temperature conversion, the routine employed a background removal filter. This filter required the auxiliary video and the scene temperature. This filter is described by the following equation:

$$T(x,y,t) = \left(\frac{T(x,y,t)}{T_{background}(x,y)} \right) T_{aux} \quad (17)$$

Where T is the temperature of the main video, $T_{background}$ the auxiliary video and T_{aux} the recorded temperature alongside the auxiliary video. This method was designed for a different experimental setup with the goal of equalising the temperature field.

4.2. Proposed methodology

The proposed methodology utilised the same camera connected in the same way, but utilised Matlab for video acquisition, instead of the Xeneth software. In spite of this, the following parameters needed to be set in the Xeneth software:

- Calibration pack set to: "none"

- Anti-bloom option set to "off"

- Gain value set to $180\,mV$

- Bias value set to $3\,nA$

- Set an register the region of interest limits

- Define and register the integration time

After the parameters were set, the camera was ready to connect to Matlab in order to start the acquisition. Since the proposed methodology employed NUC, it also required an auxiliary video, ideally two, at different temperatures near the experiment temperature. Even though these videos needed to be of a uniform temperature, the temperature value did not need to be registered.

The post-processing routine was divided in two steps: the NUC correction, as presented in section 3.1, and the ADU to temperature conversion. This conversion utilised equation 5, the emissivity and shape factor to compute the temperature value.

4.3. Experimental configuration

The experimental configuration presented aims to study the influence of a bubble formation and detachment from a superhydrophobic spot in pool boiling. The configuration aimed to study the temperature field in order to compute the heat flux utilising equation 6. As such the phenomena in study was placed over a thin metal foil, so that the thermal camera could film the phenomena from underneath.

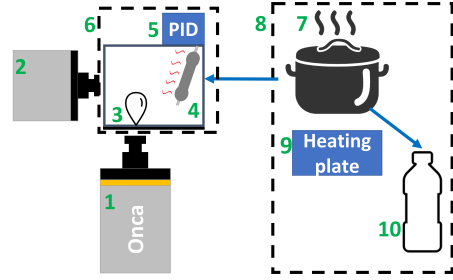The figure 5 shows the experimental setup similar to the one in [1] and [8].

Figure 5: Experimental configuration: (1) Thermal camera, (2) High-speed camera (3) Bubble phenomena (4) Electric resistance (5) PID controller (6) cell (7) Pressure pot (8) Degassing station (9) Heating plate (10) Condensation recipient

Besides the infrared camera, figure 5 index 1, a high-speed camera, phanthom v4.2, filmed the bubble formation from the side, figure 5 index 2. The fluid in this experience was distilled water, previously degassed in the degassing station, figure 5 index 8, in order to remove the dissolved gasses. The water was stored in a pressure pot, figure 5 index 7, heated with a heating plate, figure 5 index 9, to reach the boiling point at atmospheric pressure. To achieve this pressure the pot was connected to a small recipient that also stored the result of condensation, figure 5 index 10.

The pressure pot was connected to the cell, figure 5 index 6. This connection was not thermally isolated. As such the cell required electric resistances, figure 5 index 4, controlled by a PID controller, Pixsys ART121, figure 5 index 5, to control the fluid temperature. The signal to control the temperature was given by a type K thermocouple from inside the cell.

The metallic foil over which the bubble formation occurred, figure 5 index 4, was made of stainless steel AISI 304, with a thickness of $20\,\mu m$. This thickness allowed the temperature gradients to be captured by the thermal camera from outside of the cell. The heating of the plate was caused by the Joule effect, with the voltage being imposed by a power supply, model HP 6274B DC power. This allowed the foil imposed heat to be controlled.

5. Results

In this section, the experimental results are presented. Section 5.1 compares the original and treated thermograms and also compares the treated thermograms from both methodologies. Section 5.2 focuses on the new approach of heat flux computation. Besides that the location of heat flux peak utilising super resolution is also analysed.

5.1. Comparison between methodologies

In order to assess the thermogram treatment routines, the figures 6, 7 and 8, present both the original thermograms in ADU and the treated ones in degrees Celsius. A green circle is present around the bubble so that it is not mistaken by the surface defect near it.

(a) Signal before processing

(b) Signal after processing
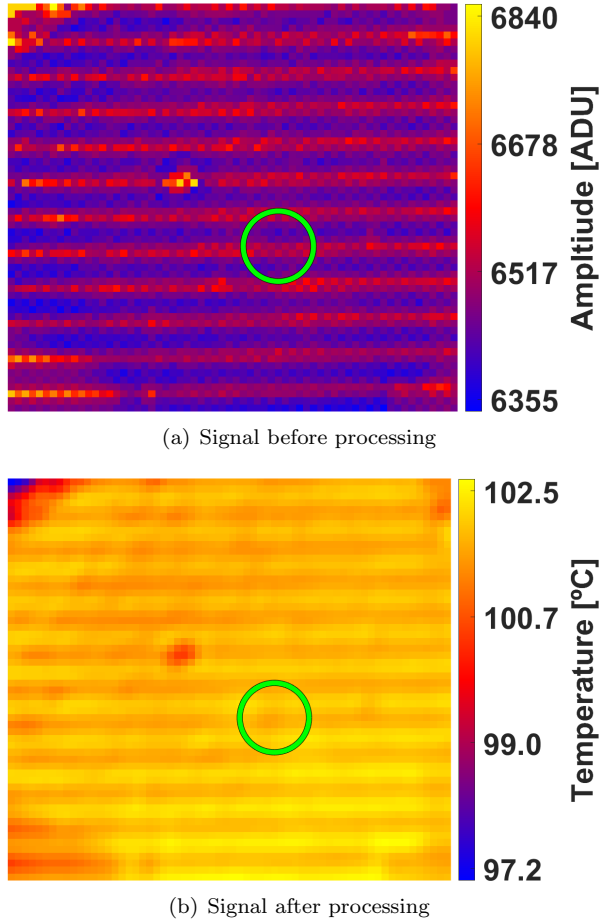
Figure 6: Previous methodology post-processing

From the three sets of images, figure 6, with the previous methodology stood out owing to its horizontal stripes present in the thermogram. These stripes were not caused by any specific thermal phenomena, appearing when the conjunction of a reduced RoI and the Xeneth offset correction were utilised. The bubble was also not distinguishable from the background difficulting further usage of the thermograms.
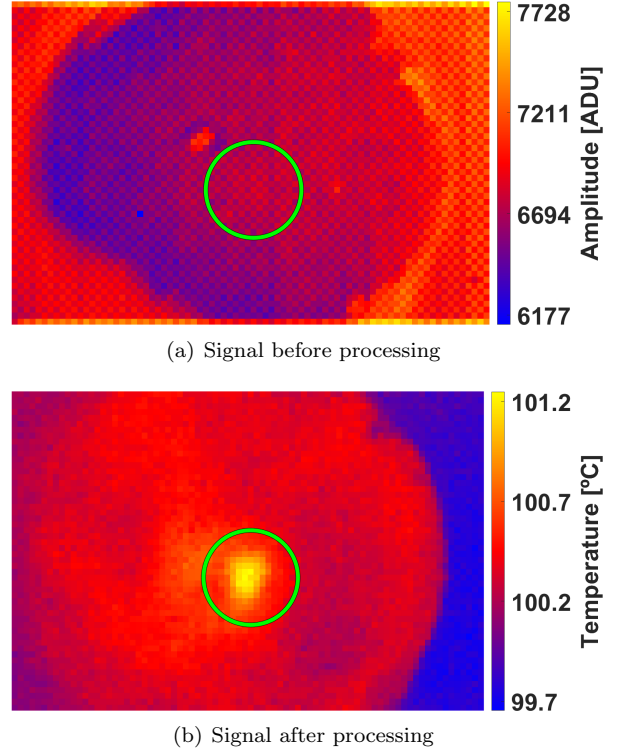

(a) Signal before processing

(b) Signal after processing

Figure 7: Proposed methodology post-processing

(a) Signal before processing
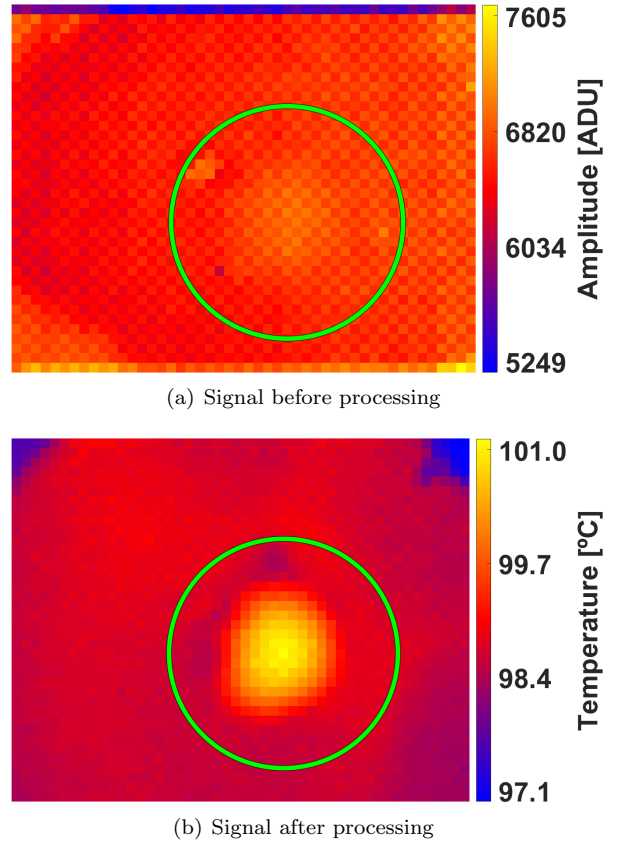

(b) Signal after processing

Figure 8: Proposed methodology post-processing with defect

The thermograms obtained with the proposed methodology, figure 7 and 8, had no horizontal stripes, since the new routine did not employ the offset correction from the Xeneth software. In the treated thermograms the bubble was clearly visible inside the circle. The pattern noise present in the original thermograms was effectivly countered by the NUC in figure 7(b). In spite of the NUC, in figure 8(b), the pattern noise was still present. This was caused by the NUC sensitivity to the position. Since the auxiliary videos were captured after several experiments were conducted, there was a slight misalignment between the auxiliary and main videos, reducing the NUC effectiveness at removing the pattern noise.

5.2. Proposed heat flux computation approach

In this section the proposed approach to the computation of heat flux is analysed.

In order to locate the position of the points analysed in this section figure 9 presents the side view from the high-speed camera and the bottom view from the infrared camera.

(a) Side view, captured with the high-speed camera
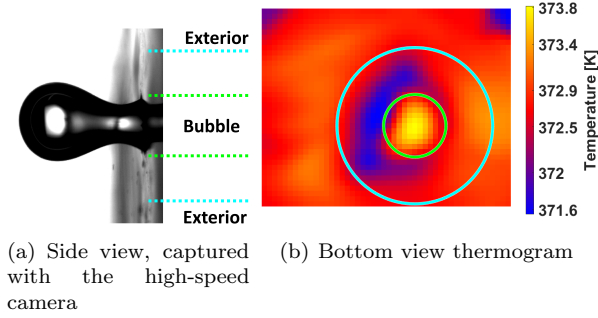
(b) Bottom view thermogram

Figure 9: Bubble regions

With these two views, two regions are defined: the bubble, inside the green circle in figure 9(b) and between the green lines in figure 9(a), and the exterior, outside of the blue circle in figure 9(b) and in the outer part of the region defined by the blue lines, figure 9(a). In order to facilitate the flux values interpretation, q_0 was set to zero, so that the points in the exterior had a heat flux near 0. This differs the bubble points where the flux was negative, with a ring of positive flux values around it.

In order to compute the heat flux with neural networks, each thermogram was fitted to a specific network, utilising the previous frame network as starting point to the adjustment of each neuron parameters. This way continuity between frames was ensured resulting in a temperature evolution without abrupt discontinuities. After the nets were fitted to the data, new thermograms were created utilising the networks, resulting in smoother data. The computation of heat flux was performed applying equation 6 to the new data. As such the heat flux

computed from the original thermograms (obtained with the proposed methodology), are referred as original, with the flux computed with neural networks being referred by the number of neurons.

Figure 10, presents the temperature and heat flux values computed with networks with $0,005\,K$ of tolerance, from a point outside of the bubble, figure 9.

(a) Temperature during an experiment for different surfaces
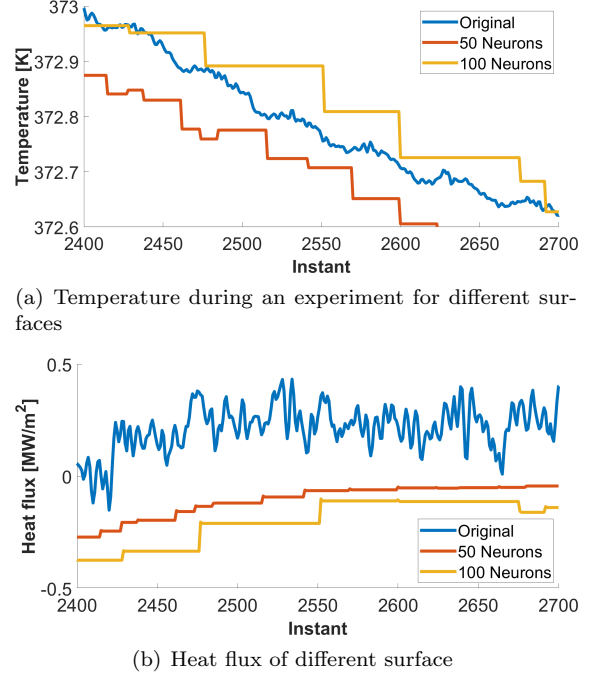

(b) Heat flux of different surface

Figure 10: Comparison of temperature and heat flux of different surfaces for an exterior point, figure 9

As expected the temperature values differ from the original thermogram, figure 10(a), on account of the tolerance value. However the heat flux value, figure 10(b), was stabler with fewer oscillations. Owing to the nature of the neural networks fitting, the networks from one frame comply with the tolerance value, creating constant heights across time. This effect was minored by the decrease in the neural networks tolerance. Figure 11, presents same point as figure 10, but with a lower tolerance of $0,0005\,K$.
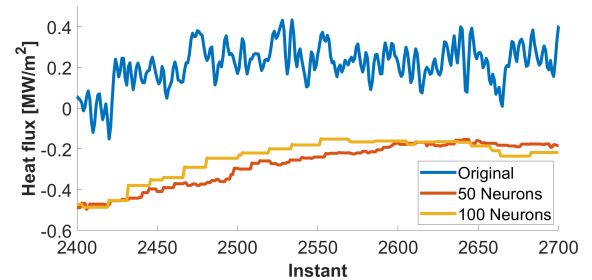

Figure 11: Detail of heat flux variation for an exterior point, figure 9

Owing to the lower tolerance, both networks were adjusted to closer values. The constant heights were still present, but with a lower difference between them comparing to figure 10(b). However the network with 100 neurons, showed more constant heights in both figure 10(b) and 11. The more complex surface allowed for a better fit, required less adaptation from frame to frame and resulted in a computed flux with more frequent constant heights.

Figure 12 presents the temperature and heat flux computed with networks with the same tolerance value, $0,0005\,K$, from the bubble point.
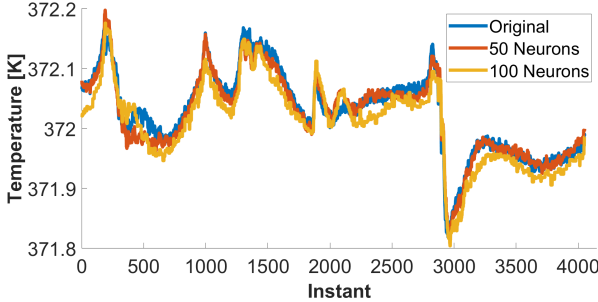
(a) Temperature during an experiment for different surfaces
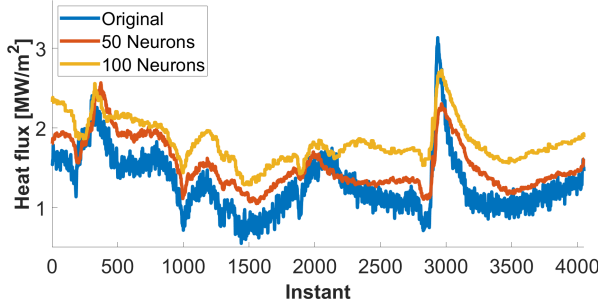
(b) Heat flux of different surfaces

Figure 12: Comparison of temperature and heat flux of different surfaces for a bubble point, figure 9

Being a point inside the bubble, figure 12(a), the temperature variations were connected to the several phases of the bubble formation and created more abrupt variation than in the exterior points. Both networks fitted the data in an adequately manner without many constant heights and closely followed the temperature values. In instant 3000 a bubble detachment took place, displaced the colder fluid from the bubble surroundings and drastically cooled the bubble region. This temperature variation created a heat flux peak, presented in figure 12(b). In spite of the network smoother data, the heat flux peak was still clearly identifiable in the data computed with the proposed approach.

The fine tuning of the number of neurons and the tolerance value was closely related to the constant heights prevalence and computation time. In order to minimise the constant heights, the neuron number and the tolerance needed to be minimised, which in turn increased the computation time. As such these parameters tuning needed to account for the required data detail and the computation time available.

With the use of neural networks, to simulate the thermograms surfaces, the created thermograms had the resolution specified by the user. This allowed for the use of super resolution techniques in order to find regions and contours of specific situations. One situation with interest for the heat flux analysis is the heat flux peak that occurs in the ring around the bubble during the bubble detachment. This phenomenon was easily timed using the high-speed camera images, but was not as clear when analysing the heat flux evolution.

Figure 13, 14 and 15 present heat flux peak regions for three different nucleations. The regions were defined using the same criteria for all the methods. Each nucleation corresponds to one primary colour: red, green, blue. The areas with two nucleations are coloured with pink, yellow and light blue. The region with the all the nucleations detected is coloured in white.
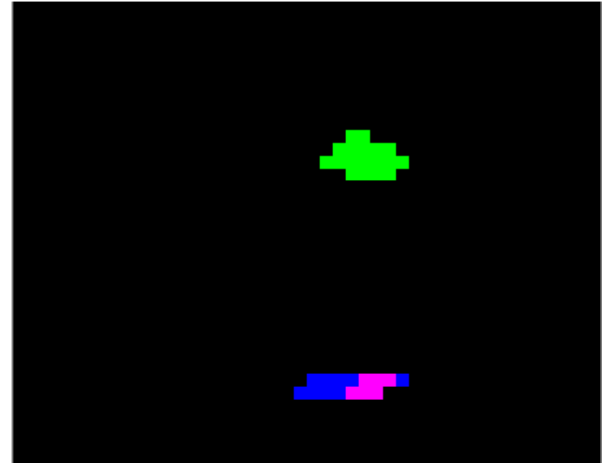

Figure 13: Original heat flux peak region

Figure 13, presents the heat fluxes regions using the heat flux computed from the thermograms without the use of neural networks. As such the regions defined were pixelated and only two of the areas with distinct nucleations were visible. With the utilisation of neural networks and maintaining the resolution, figure 14, the image was still pixelated, but a distinct third nucleation in red was visible. The increased resolution, presented in figure 15, allowed for regions to appear with non pixelated contours. In both cases, figure 14 and 15, the use of neural networks allowed for a more reliable identification of the regions, exhibiting a more ring like shape around the bubble.
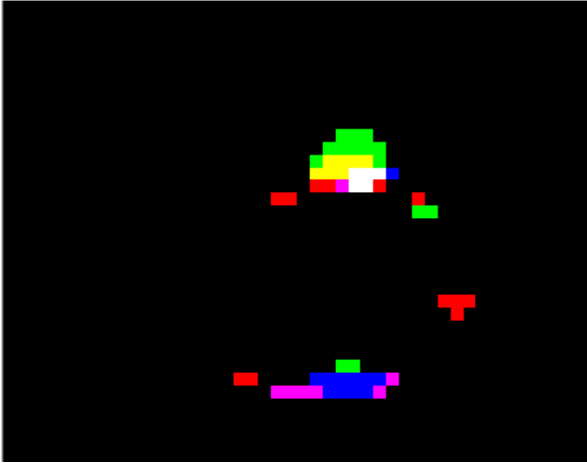
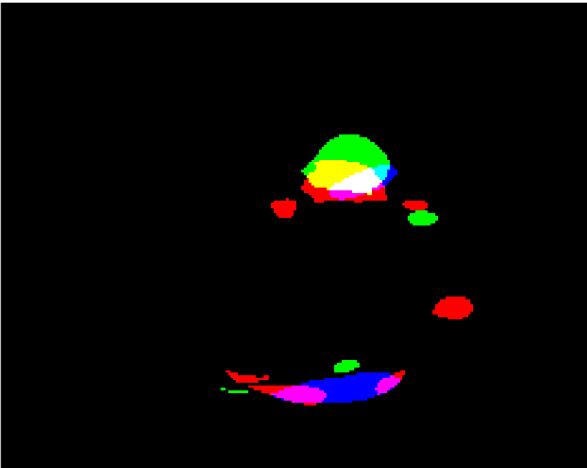Figure 14: Neural networks heat flux peak region

Figure 15: Neural networks heat flux peak region with super resolution

6. Conclusions

In this work a new approach to data acquisition and post-processing was proposed. This new approach main tool was the NUC utilised to reduce the existing pattern noise. Compared to the previous methodology the proposed one was more flexible, by not requiring a reading of the auxiliary video temperature, had a better precision, with a smaller range of temperature in the treated thermograms and an accuracy in the same range as the camera specifications.

The heat flux computation approach proposed also obtained good results, being able to reduce the noise and values oscillations in each pixel along time. Nevertheless the smoothed thermograms from the neural networks still contained the heat flux peak information, which was extracted reliably utilising super resolution methods, resulting in less pixelated regions.

6.1. Future work

Because of the several different software used in any methodology to work with this camera, a software that allows the configuration of the camera parameters, video preview and acquisition, would greatly simplify the camera usage. The heat flux computation approach showed promising results when applied to the pool boiling configuration. As such the adaptation to other types of configurations, could yield results with less noise and oscillations, improving the collected data.

References

[1] R. Cautela. Descrição dos mecanismos de ebulição em meio quiescente usando superfícies bifílicas. Master's thesis, Instituto Superior Técnico, Universidade de Lisboa, 2019.

[2] J. G. Harris and Y.-M. Chiang. Nonuniformity correction using the constant-statistics constraint: Analog and digital implementations. *Proceedings of SPIE - The International Society for Optical Engineering*, 1997.

[3] J. G. Harris and Y.-M. Chiang. Minimizing the "ghosting" artifact in scene-based nonuniformity correction. In *Infrared Imaging Systems: Design, Analysis, Modeling, and Testing IX*, 1998.

[4] N. Horny. FPA camera standardisation. *Infrared Physics & Technology*, 2003.

[5] D. L. Perry and E. L. Dereniak. Linear theory of nonuniformity correction in infrared staring sensors. *Optical Engineering*, 1993.

[6] P. Pontes. Thermographical analysis of interface heat transfer mechanisms, with high temporal resolution. Master's thesis, Instituto Superior Técnico, Universidade de Lisboa, 2016.

[7] M. Sheng, J. Xie, and Z. Fu. Calibration-based NUC method in real-time based on irfpa. *Physics Procedia*, 2011.

[8] A. Sielaff. Experimental investigation of single bubbles and bubble interactions in nucleate boiling. Master's thesis, Darmstadt, Technische Universität, 2014.